Examining Two-Way Grid Nesting for Large Eddy Simulation of the PBL Using the WRF Model

C.-H. MOENG, JIMY DUDHIA, JOE KLEMP, AND PETER SULLIVAN

National Center for Atmospheric Research, Boulder, Colorado*

(Manuscript received 9 May 2006, in final form 19 September 2006)

ABSTRACT

The performance of two-way nesting for large eddy simulation (LES) of PBL turbulence is investigated using the Weather Research and Forecasting model framework. A pair of LES-within-LES experiments are performed where a finer-grid LES covering a smaller horizontal domain is nested inside a coarser-grid LES covering a larger horizontal domain. Both LESs are driven under the same environmental conditions, allowed to interact with each other, and expected to behave the same statistically. The first experiment of the free-convective PBL reveals a mean temperature bias between the two LES domains, which generates a nonzero mean vertical velocity in the nest domain while the mean vertical velocity averaged over the outer domain remains zero. The problem occurs when the horizontal extent of the nest domain is too small to capture an adequate sample of energy-containing eddies; this problem can be alleviated using a nest domain that is at least 5 times the PBL depth in both x and y. The second experiment of the neutral PBL exposes a bias in the prediction of the surface stress between the two LES domains, which is found due to the grid dependence of the Smagorinsky-type subgrid-scale (SGS) model. A new two-part SGS model is developed to solve this problem.

1. Introduction

Large eddy simulation (LES) is a numerical modeling approach that explicitly resolves energy-containing turbulent motions that are responsible for most of the turbulent transport. It has been used intensively to examine detailed turbulence structure, to generate statistics, and to perform physical-process studies. However, most LES applications to the PBL have been limited to idealized physical conditions (e.g., PBLs over horizontally uniform surfaces; see review by Moeng and Sullivan 2003) or periodic striplike heterogeneous surfaces (e.g., Hadfield et al. 1991; Patton et al. 2005) where periodic boundary conditions are applied in the horizontal directions. Periodic boundary conditions are clearly inappropriate for PBLs that are inhomogeneous in x and/or y where turbulence fluctuations at the inflow boundary may be quite different from those at the outflow boundary. The use of periodic boundary conditions thus prevents the simulation of realistic meteorological flows over complex terrain or land use.

There are a few LESs that have used nonperiodic boundary conditions. Mayor et al. (2002) developed a perturbation recycling method to simulate an internal boundary layer associated with a cold air outbreak. At each time step during the simulation, they recycled a vertical plane of simulated turbulent perturbations at some downwind distance from the inflow boundary onto the corresponding grid point at the inflow boundary. This method is difficult to implement if the direction of the inflow keeps changing in time. Fedorovich et al. (2001) imposed uncorrelated random numbers to a laminar inflow to mimic the effect of "turbulence." Chow et al. (2006) performed LESs of PBL flow in a steep Alpine valley with specified lateral boundary conditions based on an outer-domain mesoscale flow via a one-way nesting technique.

All of the existing 1D PBL ensemble-mean models (i.e., parameterization schemes) have been developed for horizontally homogeneous PBLs where their closure assumptions and constants are based on laboratory flow data or LES solutions of horizontally homoge-

* The National Center for Atmospheric Research is sponsored by the National Science Foundation.

Corresponding author address: Dr. Chin-Hoh Moeng, MMM Division, NCAR, P.O. Box 3000, Boulder, CO 80307-3000.
E-mail: moeng@ucar.edu

DOI: 10.1175/MWR3406.1

neous PBLs. Direct applications of the existing PBL parameterizations to horizontally heterogeneous PBLs are questionable.

This problem has been recognized by the PBL community as boundary layer field experiments are shifting more and more toward emphasis on horizontally inhomogeneous PBL regimes (e.g., Doran et al. 2002; Rotach et al. 2004). However, statistical analysis of these field data is challenging. Traditional scaling laws and averaging procedures developed for horizontally homogeneous PBLs may no longer apply to these datasets. Heterogeneous surface conditions are likely to create additional length (or time) scales needed to generalize the statistical properties. Statistics measured at various sites may be too variable to be useful for the development of PBL parameterizations.

One way to tackle complex turbulent flows in weather forecast models is to explicitly resolve both turbulent and mesoscale motions of interest through two-way nesting, which allows for the feedback of turbulence effects to mesoscale prediction. With increasing computer power, this multiscale two-way nesting approach is becoming feasible in the near future. However, questions as how specified nest boundaries affect turbulent simulation and how turbulent statistics respond to grid nesting have not been explored.

In this study, we examine grid nesting for LES using the Weather Research and Forecasting (WRF) model. The Advanced Research WRF (ARW) model has state-of-the-art numerical schemes (higher-order time and advection schemes), which are crucial for turbulence simulation. The WRF model also has a two-way nesting capability and can accommodate multiple embedded nests, which are attractive for future studies where LES can be nested within several layers of domains in which mesoscale motions gradually scale down to turbulent motions. WRF is designed for massively parallel computers with two-dimensional grid partitioning in the horizontal plane, and thus has the potential of performing very high resolution and very large domain simulations. Another advantage of using the WRF model is its inclusion of real-world terrain and land-use data as well as real atmospheric conditions for future real-world PBL studies.

Two-way nesting allows for interaction between outer and inner domains. In WRF, the two-way nesting is performed as follows. The parent (outer) domain is first integrated one time step. Its time- and space-interpolated values are then specified on the nest boundaries while the nest (inner) domain is advanced with the small-grid time interval (typically three steps for an outer-to-inner-domain ratio of 3:1) to reach the parent domain's time level. Then the interior values of the nest domain are averaged back to the parent domain, overwriting the parent domain solution in this overlapped region. See Skamarock et al. (2005) for the details of the procedure.

Two-way nesting has served many applications, but is seldom applied to LESs. Sullivan et al. (1996) looked at vertical nesting where both fine and coarse domains are required to have the same horizontal extent in order to still use periodic boundary conditions in both x and y. In this study, we look at horizontal nesting where the inner domain covers just a portion of the horizontal extent of the outer domain, and the nested-domain LES no longer uses any periodic boundary conditions. For weather prediction applications, nested domains are often specified such that events of interest occur away from the nest boundaries to minimize possible numerical problems due to nest boundary conditions (e.g., hurricane simulations).

For LESs, turbulence in the PBL extends throughout the nested domain, even at the nest boundaries. Any numerical noise excited by lateral boundary conditions propagates quickly into the nest domain due to turbulent mixing. This problem is further complicated in the WRF model in that it solves the fully compressible equations. Unlike most PBL LESs that solve an incompressible Boussinesq system with $\nabla \cdot \mathbf{u} = 0$ (Deardorff 1974), the compressible WRF model generates acoustic waves. Near the nest boundaries, the $\nabla \cdot \mathbf{u} = 0$ condition (for shallow, incompressible PBL motion) is likely to be violated, which then excites acoustic waves. How acoustic modes excited at the nest boundaries affect turbulence simulation is unclear.

To test the two-way nesting capability for LES and to validate the solution, we design LES-within-LES experiments where one LES is nested within the other and the turbulence within both LESs are driven by the same forcing in the same environment. The only differences between the two LESs are 1) the outer LES domain covers a larger horizontal extent and has a coarser horizontal resolution than the inner LES domain and 2) the outer-domain LES uses a periodic boundary condition in x and y (like conventional PBL LESs), while the inner-domain LES uses a specified lateral boundary condition based on the outer-domain flow. We examine two idealized PBL turbulent flows whose structure and statistical behavior are well documented so we can verify the solution.

The LES-within-LES experiments provide a useful tool to explore the nesting capability. With the same forcing and environmental conditions, the two LESs are expected to generate similar turbulent flow fields. Previous LES studies suggest that most of the relevant statistics (e.g., mean, flux, and variance profiles) are

insensitive to grid resolution—as long as LES grid size lie in the inertial subrange over the bulk PBL. This is evidenced by comparing the results from four coarse-grid LESs (with a horizontal size of 160 m) reported by Nieuwstadt et al. (1993) and those of a fine-grid LES (with a horizontal grid size of 50 m) performed by Schmidt and Schumann (1989) for the free-convective PBL, and by comparing the 40^3 LESs reported by Andren et al. (1994) and a 96^3 LES performed by Moeng and Sullivan (1994) for the neutral PBL. If the specified nest boundary conditions function properly, the turbulent flow will blend smoothly across the two domains. More importantly, the LES-within-LES experiment provides a framework for rigorous testing of the subgrid-scale (SGS) model. Because the resolved-scale (RS) contribution to the total fluxes or variances is larger in the fine-grid domain than in the coarse-grid domain, the SGS model is solely responsible for generating the remaining amount of turbulent transport. Otherwise, different turbulent transports of heat and momentum would generate different flow fields in the two LES domains, and with two-way nesting such differences would generate mean temperature or velocity gradient across the nest boundaries.

2. The model and experiment setup

a. The PBL regimes

For validation purposes, we choose two idealized PBL regimes: free-convection and pure shear-driven PBLs. The free-convection case has zero mean wind and the only driving force for turbulence is uniform surface heating. This PBL regime (denoted as F) has been simulated by many LES practitioners (e.g., Schmidt and Schumann 1989; Nieuwstadt et al. 1993) and its flow structure and statistics are well documented and shown to agree well with convective tank experiments (Willis and Deardorff 1979). Its most significant flow feature is the spokelike, irregular cellular structure near the surface and its statistics are known to scale with the PBL depth z_i and the convective velocity $w_* \equiv [(g/T_0)Q_0 z_i]^{1/3}$, where Q_0 is the surface heat flux, g gravitational acceleration, and T_0 is the reference temperature (Deardorff 1972; Lenschow et al. 1980). For example, the vertical-velocity variance normalized by w_*^2 has a peak of 0.4–0.5 at about $0.4z_i$ and the u and v variances are about 0.2 w_*^2 in the middle of the PBL. For our case, the surface temperature is set to be 5 K warmer than the air temperature at the initial time; a significant amount of upward surface heat flux, which drives turbulence, is calculated in the surface layer subroutine using Monin–Obukhov (MO) theory. This case is used to examine whether the same surface heating will drive the same turbulent flows and transport the same amount of heat into both PBL domains—without the mean wind advection.

The shear-driven PBL (or so called neutral PBL, denoted as S) is driven by large-scale pressure gradient forces, specified as a geostrophic wind. Because the drag slows the wind down near the ground, a strong shear develops near the surface, which can drive turbulence. The structure and statistics of the neutral PBL are also well documented (e.g., Andren et al. 1994; Moeng and Sullivan 1994; Lin et al. 1997). The most significant structure is the near-surface streaky feature of high–low speed fluid, roughly aligned with the mean wind near the surface. The velocity scale for the neutral PBL is the surface friction velocity (u_*) and, with a capping inversion, the length scale is the PBL depth z_i. Previous studies show that in wall-bounded, shear-driven turbulence, the peak value of the streamwise velocity variance occurs near the walls and is about 6–8 u_*^2. In our simulation, we set the geostrophic wind to $U_g = 15\ \mathrm{m\,s^{-1}}$ and $V_g = 0$, similar to the setup by Moeng and Sullivan (1994) for comparison. To effectively spin up the turbulence field, we initialized this simulation from a weakly convective PBL flow, generated by imposing a small surface heat flux, $30\ \mathrm{W\,m^{-2}}$ as a bottom boundary condition in the vertical diffusion. After about an hour of simulation time, we reset the surface heat flux to zero and ran the model for another three–four simulation hours to generate a neutral PBL. Data from the last 2 hours of simulation are used to compute statistics. This integration time may not be long enough to generate a quasi-steady neutral PBL, but is adequate for the purpose of this study.

b. LES-within-LES experiment design

We adopt the idealized dry version of the WRF ARW with the following changes and experimental setup. All physics options (microphysics, cumulus, PBL parameterization, land processes, radiation, damping layer, vertical-velocity damping, etc.) are turned off—except the diffusion and surface layer schemes. The predicted friction velocity (UST) and surface heat flux (HFX) from the surface layer scheme are passed on to the turbulent diffusion scheme where they modify the momentum and potential temperature fields at the lowest grid level. The model configuration in the horizontal plane is shown in Fig. 7.3 of Skamarock et al. (2005) where the inner domain can be nested at an arbitrary location. With periodic lateral boundary conditions in the outer domain, our results are independent of the nest location.

We choose different horizontal grid sizes for the two cases because the energy-containing eddies are typi-

cally larger in buoyancy-driven turbulence than in shear-driven turbulence. For case F, the horizontal grid size is $\Delta x = \Delta y = 150$ m in the outer domain (similar to that used by Nieuwstadt et al. 1993) and $\Delta x = \Delta y = 50$ m in the nest domain (which is similar to that used by Schmidt and Schumann 1989 and Moeng and Sullivan 1994); both domains use 100 grid points in x and y, respectively. For case S, $\Delta x = \Delta y = 60$ m (similar to that used in Andren et al. 1994) with 100×100 grid points in the outer domain, while in the nest domain $\Delta x = \Delta y = 20$ m (similar to that used by Moeng and Sullivan 1994) with 121×121 grid points. (The 3:1 grid ratio between the outer and nest domains is typical for WRF.) Within this grid resolution range, previous LES studies show that the ensemble-mean statistics (e.g., total fluxes and velocity variances) remain similar. Thus, we expect the net statistics—the sum of RS and SGS contributions—to be similar in both domains.

No vertical nesting is available in WRF, so we use a vertical extent of 2 km for both domains with 100 equal-spaced grid levels for case F and 200 for case S. Hence, $\Delta z \sim 20$ m in case F and $\Delta z \sim 10$ m in case S. (WRF uses a mass coordinate, so the vertical grid size is not exactly equal everywhere.)

In the time-split integration scheme used in the ARW, we set the large time step (for low-frequency motions) Δt to 1 s and ⅓ s for the outer and inner domains, respectively, for both cases. The small time step (for high-frequency acoustic modes) Δt_s must satisfy the general rule of $c\Delta t_s/\Delta x < ½$ where $c \sim 300$ m s^{-1} is the sound speed. We found that the WRF model generates too much acoustic noise near the nest boundaries if the number of sound steps per large time step is much larger than 10, perhaps because the two domains do not communicate during the small time step integration. Thus, we limit our large time step to 1 s (and ⅓ s) for outer (and inner) domains for both cases, so $\Delta t/\Delta t_s$ can be set to 6.

The initial temperature sounding for case F is similar to that used by Moeng and Sullivan (1994) where the potential temperature is 300 K below an initial PBL height (z_{i0}), increases by a total of 8 K over an inversion depth of 150 m, and increases with a lapse rate of 3 K km^{-1} above the inversion. The sounding is the same for case S except that the inversion strength is 3 K over a depth of 100 m. The capping inversion is imposed to limit the growth of the PBL and hence limits the growth of the energy-containing eddy size. For case F we set $z_{i0} = 1$ km, and for case S $z_{i0} = 500$ m. The initial mean wind is zero for case F and set to U_g throughout for case S. The roughness length is 0.16 m and the Coriolis parameter $f = 10^{-4}$ s^{-1} for both cases.

The numerics in the WRF ARW model differ significantly from those used in the National Center for Atmospheric Research (NCAR) LES code (Moeng 1984): the ARW model solves fully compressible equations on a mass coordinate and uses finite differencing in horizontal and vertical, while the NCAR LES code solves incompressible equations on a height coordinate and uses Fourier representations in the horizontal plane. Nevertheless, LES intercomparison studies (Nieuwstadt et al. 1993; Andren et al. 1994) suggest that first- and second-moment statistics of the simulated turbulent flows are insensitive to the numerical techniques used.

We choose the fifth-order finite-differencing advection scheme for horizontal advection, the third order for vertical advection, and the third-order Runge–Kutta scheme for time integration. Higher-order advection schemes preserve the accuracy of small-scale features, while odd-order schemes have a small amount of implicit diffusion preventing an unrealistic peak at the small-scale end of the energy spectrum. With the Courant number we use here, the numerical diffusion is very small. For acoustic wave damping, we use the standard damping coefficients, with the 3D divergence damping coefficient set to 0.1, the external wave filter coefficient set to 0.01, and the small time step off centering coefficient set to 0.01. For the surface layer, we use MO theory to predict UST and HFX.

Other minor changes made to the standard WRF idealized run are the following. In the initialization, we perturb the initial temperature at the lowest four levels with a random field having values between −0.1 and 0.1 K. For case F, we set the surface temperature TSK to be 5 K higher than the initial temperature at the first grid level. The diffusion uses the surface stress and surface heat flux (UST and HFX) predicted from the surface layer scheme. We eliminate Deardorff's wall correction to the dissipation coefficient, which has been shown to be unnecessary as long as LES has adequate grid resolution. We also relocate the grid points for SGS turbulence kinetic energy (TKE) and SGS eddy viscosity and diffusivity for vertical diffusion to w levels (full-grid levels) to improve numerical accuracy (Nieuwstadt et al. 1993), although the results are not sensitive to this relocation.

c. *The diffusion scheme: A new two-part SGS model*

The major change we made to the WRF code is in the SGS diffusion routine. For LESs, the SGS mixing process includes horizontal and vertical mixing. In WRF there are several ways to compute the 3D SGS eddy viscosity and diffusivity (K_M and K_H); our new option is discussed below.

The SGS mixing in LES represents the net effect of all eddies that are smaller than the grid resolution; hence, by construction the SGS TKE is larger in the outer (coarse) domain than in the inner (fine) domain. Therefore, we cannot simply adopt the SGS TKE predicted by the outer domain to specify the SGS TKE at the boundaries of the inner domain. In the standard WRF version using the TKE option, the SGS TKE is set to zero at the nest boundaries, which is also incorrect. A proper way to relate the SGS TKE between two LESs with different grid sizes is to adopt the Germano's identity (Germano et al. 1991; Sullivan et al. 1996), but that scheme is computationally costly. To avoid the need of specifying SGS TKE at the nest boundaries, we neglect the time change and advection terms in the SGS TKE budget (which are small anyway) such that the total production (shear plus buoyancy) is exactly balanced by the molecular dissipation as

$$\frac{1}{2}K_M D_{ij}^2 - K_H \frac{g}{\theta_0}\frac{\partial \theta}{\partial z} = \epsilon = c_\epsilon \frac{e^{3/2}}{\ell}, \tag{1}$$

where the strain rate D_{ij} in WRF is defined as

$$D_{ij} = \frac{\partial u_i}{\partial x_j} + \frac{\partial u_j}{\partial x_i}, \tag{2}$$

(which is a factor of 2 different from the conventional form), θ_0 is reference potential temperature; θ, potential temperature; e, SGS TKE; c_ϵ, dissipation coefficient; and ℓ, a SGS length scale. This diagnostic TKE approach is basically the Smagorinsky first-order closure option in the ARW model but the following modifications are made to account for the stability dependence of the SGS length scale.

The usual SGS eddy viscosity and diffusivity (K_M^{sgs} and K_H^{sgs}) are defined as

$$K_M^{\text{sgs}} = c_K \ell \sqrt{e}, \tag{3}$$

and

$$K_H^{\text{sgs}} = \left(1 + \frac{2\ell}{\Delta s}\right) K_M^{\text{sgs}}. \tag{4}$$

Here Δs is the filtered length scale taken as the cube root of the grid volume,

$$\Delta s = (\Delta x \Delta y \Delta z)^{1/3}, \tag{5}$$

and the SGS length scale ℓ is suggested by Deardorff (1980) to take into account the local stratification effect, defined as

$$\ell = \min\left[0.76 e^{1/2}\left(\frac{g}{\theta_0}\frac{\partial \theta}{\partial z}\right)^{1/2}, \Delta s\right]. \tag{6}$$

There are two closure constants: the dissipation coefficient c_ϵ in (1) and the diffusion coefficient c_κ in (3). Following Moeng and Wyngaard (1988) we set $c_\kappa = 0.1$ and $c_\epsilon \sim 0.19 + 0.74\ell/\Delta s$. These values are smaller than the default values used in WRF, which are tuned for mesoscale cloud simulations (Takemi and Rotunno 2003).

From (1), (3), and (4), the SGS TKE can be written as

$$e = \frac{c_K \ell^2}{c_\epsilon}\left[\frac{D_{ij}^2}{2} - \left(1 + \frac{2\ell}{\Delta s}\right)\frac{g}{\theta_0}\frac{\partial \theta}{\partial z}\right], \tag{7}$$

which is used to calculate the SGS TKE. The computed SGS TKE is then used in (3) and (4) to calculate the Smagorinsky's component of K_M and K_H.

Another modification to the diffusion model [i.e., adding a second part of K_M (and K_H) to the Smagorinsky model near the surface as described below] is made for two intended reasons. First, there is a long-standing problem that the predicted mean wind from LES of the neutral PBL often deviates from the well established MO similarity form in the surface layer. This deficiency was first mentioned by Mason and Thomson (1992) where they proposed a correction by introducing stochastic backscattering in their Smagorinsky SGS model. Adding stochastic backscattering effect into LES is computationally costly and generates random noise near the surface. Instead, Sullivan et al. (1994) proposed a two-part SGS eddy viscosity model, in which they augment the conventional Smagorinsky eddy viscosity by adding a mean-field eddy viscosity "devised to recover law-of-the-wall behavior in the absence of any resolved turbulence." With the two-part SGS model, they were able to produce an LES field that obeys MO similarity in the surface layer. But adopting their mean-field eddy viscosity model requires computations of horizontally averaged wind and strain rate, which may greatly reduce the computational efficiency of WRF because of the two-dimensional horizontal grid partitioning in the MPI environment. The use of horizontally averaged eddy viscosity also limits our future applications to PBLs over complex terrain.

The second and more urgent reason for modifying the Smagorinsky K_M is that using the Smagorinsky model alone generates a bias in surface friction velocity between the outer and inner domains as we will show in the next section. To alleviate this problem, we develop a two-part SGS eddy viscosity model, which is similar to that proposed by Sullivan et al. (1994) but with a different second part of SGS eddy viscosity. Instead of using a mean-field eddy viscosity, we propose a local, fluctuating eddy viscosity (denoted as K_M^{wall}) to recover the law-of-the-wall behavior at all grid points at the first

full-grid level $z = \Delta z$. The total SGS eddy viscosity is expressed as

$$K_M = K_M^{\text{sgs}}\gamma + K_M^{\text{wall}}(1 - \gamma), \quad z < 2\Delta_h, \tag{8}$$

where Δ_h is the largest of Δx and Δy and γ is an isotropy factor, which is treated differently from that of Sullivan et al. We simply assume it increases linearly from $\gamma_1 = 0.2$ at $z = \Delta z$ to 1 at $z = 2\Delta_h$. The γ value at the first full grid level is empirically determined; a sensitivity test using $\gamma_1 = 0.4$ shows no significant difference.

The K_M^{wall} part is turned on only below $z = 2\Delta_h$. For small turbulent eddies that are nearly isotropic in shape (i.e., those with the same characteristic length scale in x, y, and z) they are poorly resolved below the horizontal grid resolution, which is typically taken to be $2\Delta_h$. It is in this thin layer, where the Smagorinsky-type of SGS model is questionable, that we augment the Smagorinsky eddy viscosity K_M^{sgs} with a grid-independent eddy viscosity K_M^{wall}, as described below.

Following Sullivan et al. (1994), we first force the vertical gradient of local u at the first w level ($z = z_1 = \Delta z$) to obey the law-of-the-wall:

$$\left(\frac{\partial u}{\partial z}\right)_{z_1} = \frac{u_*}{\kappa z_1}\phi_m, \tag{9}$$

where ϕ_m is the MO stability function. To avoid the need to calculate ϕ_m in the diffusion routine, we will set $\phi_m = 1$. That means we will apply the two-part SGS model only to near-neutral PBLs where both problems mentioned above are most significant (Sullivan et al. 1994 and later in the results section). For near-neutral PBLs with small $z/|L|$ (where L is the MO length scale), $\phi_m = 1$ is a reasonable assumption. The surface stress $\tau_{ij}^* \equiv -u_*^2$ can be expressed in term of eddy viscosity as

$$\tau_{ij}^* = -[K_M^{*\text{sgs}}\gamma_1 + K_M^{*\text{wall}}(1 - \gamma_1)]D_{ij}^*, \tag{10}$$

where D_{ij}^*, the strain rate at the z_1 level, is dominated by the vertical shear term, and hence $D_{ij}^* \sim (\partial u/\partial z)_{z_1}$. From Eqs. (9) and (10), we have

$$K_M^{*\text{wall}} = \frac{\kappa u_* z_1 - K_M^{*\text{sgs}}\gamma_1}{1 - \gamma_1}, \tag{11}$$

which is K_M^{wall} at the lowest level z_1. The K_M^{wall} above z_1 is then computed, following Sullivan et al. (1994), as

$$\frac{K_M^{\text{wall}}}{K_M^{*\text{wall}}} = \frac{\sqrt{D_{ij}D_{ij}/2}}{\sqrt{D_{ij}^*D_{ij}^*2}}, \tag{12}$$

or

$$K_M^{\text{wall}} = K_M^{*\text{wall}}\frac{\kappa z_1}{u_*}\sqrt{D_{ij}D_{ij}/2}. \tag{13}$$

In summary, for PBL regimes with small $z/|L|$ (here we use 0.1 as a criterion), we apply the two-part SGS eddy viscosity as described in (8) where K_M^{wall} is obtained from (13) and K_M^{sgs} from (3).

3. Results

The LES version of WRF was first examined without nesting (i.e., running as a typical single-domain LES with periodic boundary conditions in both x and y). The results from two single-domain LESs using a grid mesh of 150 m × 150 m × 20 m and 50 m × 50 m × 20 m, separately, for case F are shown in Fig. 1. The overall features are comparable to previous LESs (e.g., Schmidt and Schumann 1989; Nieuwstadt et al. 1993), although the predicted heat fluxes at the PBL top are larger than previous LESs, which often produced a heat flux at the PBL top about −0.2 of the surface flux. The fine-grid LES also produces larger velocity variances compared to the coarse-grid LES. The SGS variances (which are taken to be 2/3 of the SGS TKE, assuming isotropy for small eddies) of the coarse-grid LES is still larger than that of the fine-grid LES, as expected, but the difference in the middle of the PBL is not large enough to compensate for the difference in their RS contributions. The difference in the total variances between the two LESs is unexpected, suggesting sensitivity of variances to grid resolution; nevertheless, their values (where vertical-velocity variance peaks at 0.4–0.5 w_*^2 at $z \sim 0.4z_i$ and the u and v variances are about 0.2 w_*^2 in the middle of the PBL) are within the uncertain range of field measurements (e.g., Lenschow et al. 1980) and previous LESs (Nieuwstadt et al. 1993).

Figure 2 compares the momentum flux and velocity variances from two single-domain LESs for the shear-driven PBL. The coarse- and fine-grid LESs use a grid mesh of 60 m × 60 m × 10 m and 20 m × 20 m × 10 m, respectively; both LESs adopt the new two-part SGS model described in section 2c. As anticipated, the coarse-grid LES produces a smaller RS contribution (i.e., resolving less) but a larger SGS contribution than the fine-grid LES. The coarse-grid LES predicts a surface friction velocity that starts at about 0.45 m s^{-1} at the beginning of hour 3 and then reaches 0.5 m s^{-1} during the fourth hour of simulation, while the fine-grid LES shows $u_* \sim 0.5$ m s^{-1} persistently over the last two simulations hours. The three velocity variances (RS plus SGS), normalized by u_*^2, are given in Fig. 2b. The difference in the u-variance (thick solid and dotted curves) between the two single-domain LESs is unexpectedly large, larger than previous LESs with the same resolutions (cf. Andren et al. 1994; Moeng and Sullivan 1994). The near-surface peak value of the u variance of

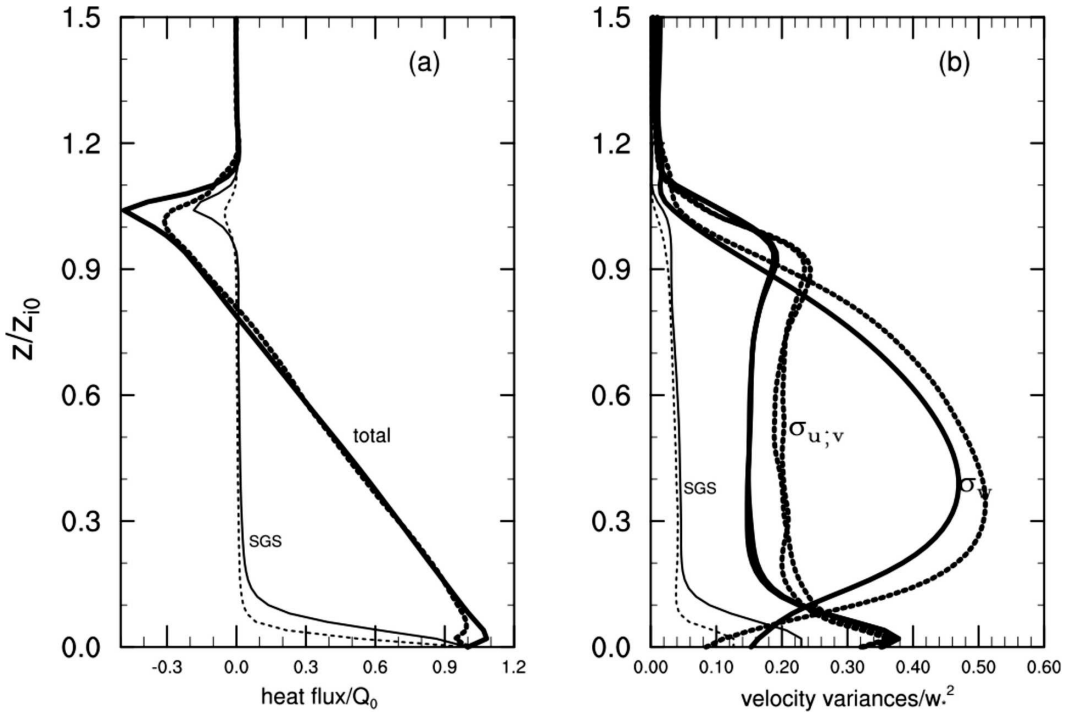

FIG. 1. Comparison of the vertical profiles of time-averaged (between hours 1.5 and 2.5 of the simulation) (a) heat flux and (b) velocity variances between two single-domain LESs of case F. The solid curves are from the coarse-grid LES and the dotted curves are from the fine-grid LES.

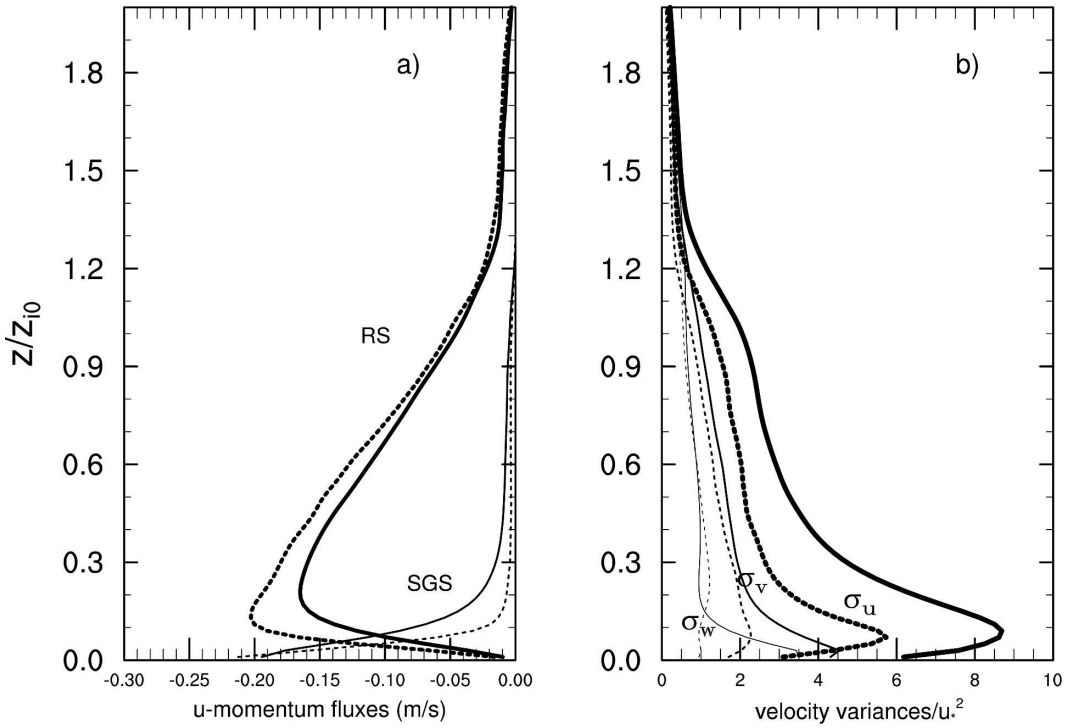

FIG. 2. Comparison of the vertical profiles of (a) *u*-momentum flux and (b) velocity variances between the two single-domain LESs of case S. The solid curves are from the coarse-grid LES and the dotted curves are from the fine-grid LES.

the coarse-grid LES is about $8 \sim 9\ u_*^2$, while that of the fine-grid LES is about $6\ u_*^2$, the latter being closer to that reported in the earlier studies using the NCAR LES code (Moeng and Sullivan 1994; Sullivan et al. 1994). Whether this strong sensitivity of u variance to grid resolution is a unique feature of WRF LES is not clear and may require further investigation. Kravchenko and Moin (1997) also reported large sensitivity of velocity variances to data sampling and numerics.

The proposed two-part SGS model does not solve the law-of-the-wall deficiency as we had anticipated. Figure 3 shows the nondimensional velocity gradient Φ_M, defined as

$$\Phi_M = \frac{\kappa z}{u_*} \frac{\partial |\mathbf{V}|}{\partial z}, \tag{14}$$

where $|\mathbf{V}|$ is the horizontal wind speed and $\kappa = 0.4$ is the von Kármán constant. Like most LESs (Andren et al. 1994), this LES still overpredicts Φ_M in the surface layer (which should be 1 below $\sim 0.1 z_i$ according to the law of the wall for neutral flows). Nevertheless, the finer-grid LES produces a better profile compared to the coarse-grid LES, converging to the logarithmic profile. The mean-wind-profile deficiency in shear-driven surface layer is a long-standing problem for PBL LES. Different solutions have been proposed (e.g., Mason and Thomson 1992; Sullivan et al. 1994; Porte-Agel et al. 2000), which did decrease the vertical shear near the surface and bring the predicted Φ_M closer to the logarithmic profile, but the underlying cause for the overpredicted mean shear near the surface is still not completely understood (Juneja and Brasseur 1999). We will leave this near-wall problem for future study because our purpose here is to examine the two-way nesting capability of LES.

With two-way nesting, the LES-within-LES experiment was first performed without any relaxation zone along the nest boundaries and this led to poor results; significant amounts of numerical noise were generated along the nest boundaries. Only with the recent implementation of a relaxation zone (in version 2.1.1) inside the nest boundaries, does the simulated turbulent flow begin to behave reasonably. The relaxation zone of the nested boundary is identical to that used previously for specified lateral boundary conditions at the outer-most domain for real-data case simulations (see Fig. 6.1 in Skamarock et al. 2005 for details). The relaxation zone is five grid intervals wide with a relaxation coefficient decreasing linearly inward from the nested boundary. In addition to the relaxation term, there is a smoothing term that is similarly ramped. The relaxation is toward the time and space interpolated parent domain values of all prognostic fields.

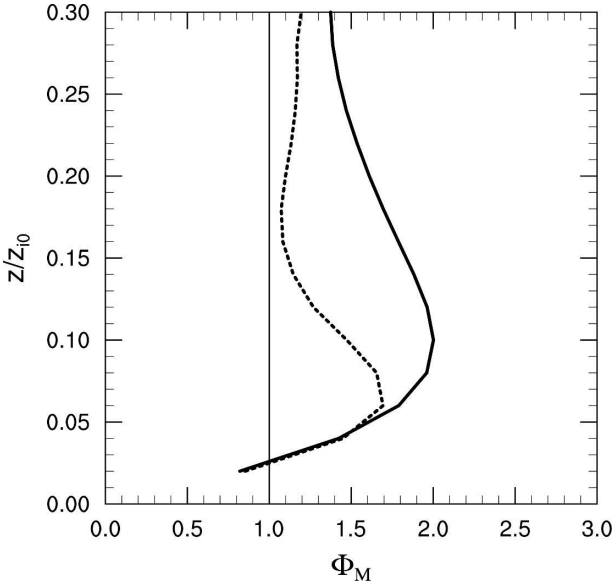

FIG. 3. Vertical profiles of the normalized mean wind gradient in the surface layer from the two single-domain LESs of case S. The solid curves are from the coarse-grid LES and the dotted curves are from the fine-grid LES.

Even with the relaxation zones, we still encounter two major problems, which are reported below, along with our solutions to these problems.

a. Mean temperature bias

From case F, we first noticed that the mean temperature tended to become warmer in the nested domain than in the outer domain. With this warm bias, the nested domain produced an undesired mean upward motion that persists for a few hours. Figure 4 shows the time evolution of (Fig. 4a) the horizontally averaged potential-temperature differences between the inner and outer domains and (Fig. 4b) the horizontally averaged vertical velocity of the inner domain during a 4-h simulation. (The mean vertical velocity in the coarse-grid domain remains zero as expected due to the use of periodic lateral boundary conditions.) The mean bias persists for about 3 h. Even though the magnitude of the mean temperature bias is very small, the mean vertical-velocity bias is on the order of a few tenths of a meter per second, which is the order of the vertical-velocity fluctuations of turbulence. Experimenting with different setups (e.g., different SGS length scale, one-way nesting, different grid resolutions, delayed start-up time for nest domain, and double precision runs) indicated that this mean temperature or vertical-velocity bias could go either way—a warmer nest domain with a

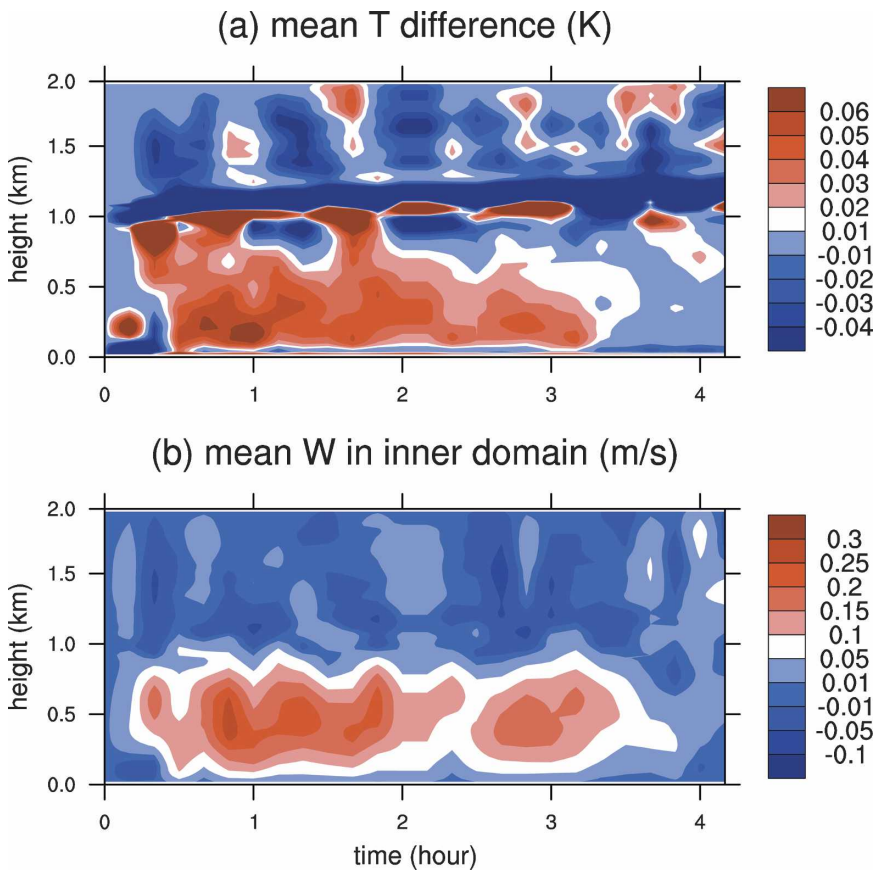

FIG. 4. Contours of (a) the mean temperature difference between the outer and inner domains and (b) the mean vertical velocity in the inner domain during a 4-h simulation of the free convective PBL.

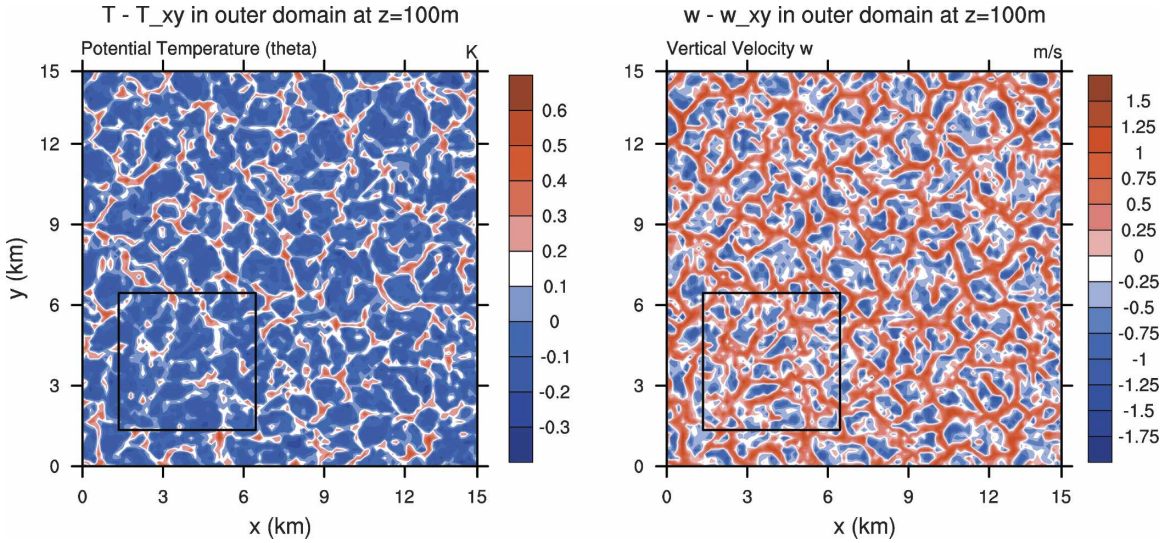

FIG. 5. Contours of (left) θ and (right) w fluctuations on a horizontal cross section at $z = 100$ m from the outer domain at the end of the ~2.5 h of the free-convective PBL simulation.

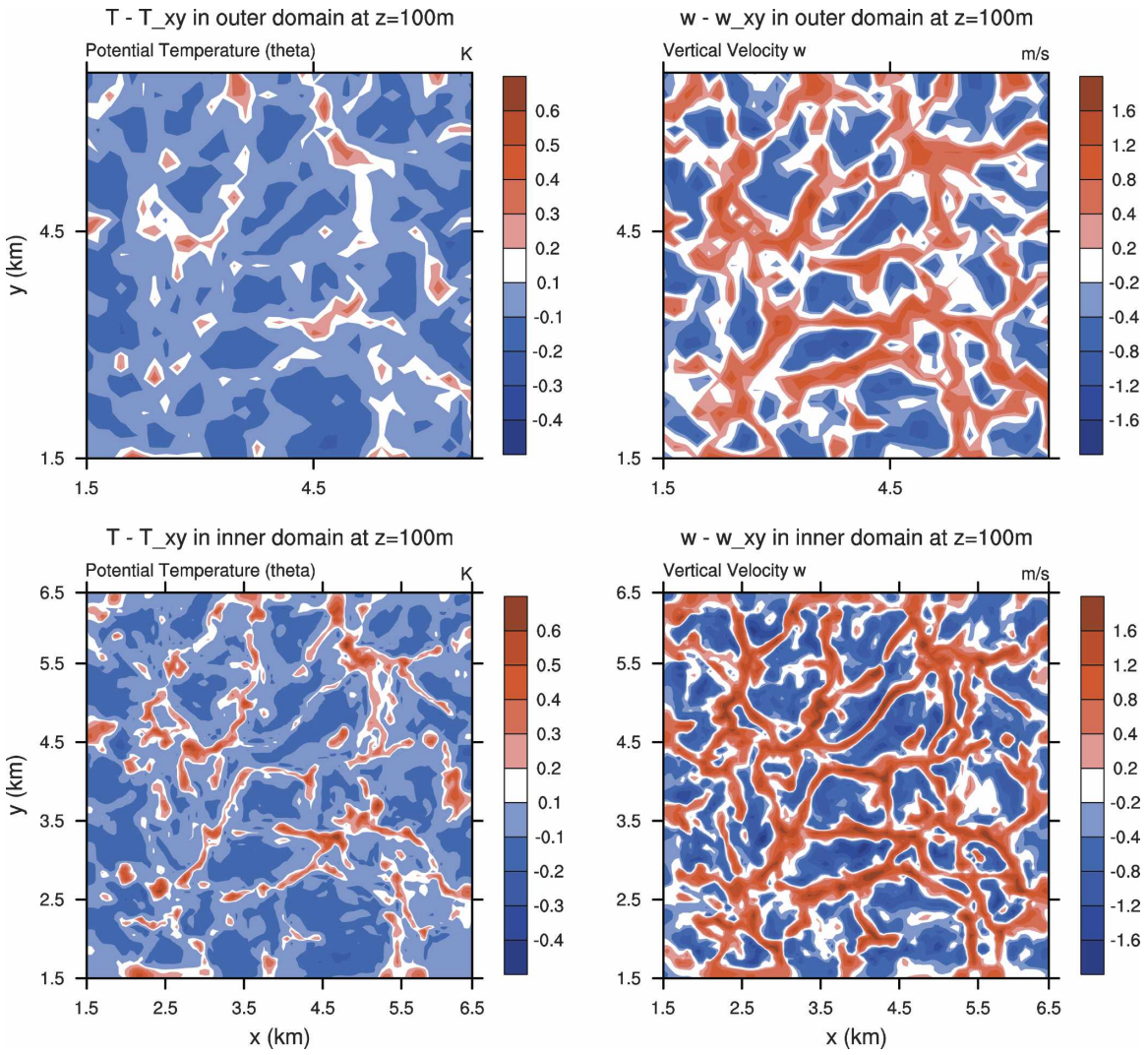

FIG. 6. Same contour plots as in Fig. 5, but for the nest region only: (top) the outer domain and (bottom) the inner domain.

mean upward motion or a colder nest domain with a mean downward motion.

We traced this bias problem to the horizontal extent of the nest domain. The first case F run was performed using a nest domain of about 2.5 km in both x and y. With the PBL depth of about 1 km, the domain resolved only a couple of large eddies. The few resolved large eddies, which could be either updrafts or downdrafts, were responsible for most of the vertical heat transport. If at the early stage of simulation the nest domain happens to be dominated by a few updrafts, they quickly produce a warmer PBL in the nest domain. With two-way interaction, a mean circulation develops across the two domains, just like a heated-island effect, and the warm bias can persist for several hours. (With one-way nesting, the flow in the outer domain is not influenced by the nested LES and hence does not generate a mean circulation to compensate for the bias; in the one-way nesting situation, the few dominant eddies inside the nest LES are sometimes updrafts and sometimes downdrafts, which even out when calculating statistics with a long time averaging.)

Through experimentation, we found that using a nest domain with a much larger horizontal extent prevents this mean temperature (or vertical velocity) bias from occurring. With a larger nested domain, there is an adequate sample (at any instant) of random resolved-scale eddies, updrafts and downdrafts, to eliminate the bias. The results we show in this paper are from two-way nesting runs with the inner domain of $5z_i$ (i.e., 5 km) in x and y; the mean temperature and vertical-velocity bias between the outer and inner domains in this run is negligibly small (i.e., the features shown in Fig. 4 disappear).

Figure 5 shows the temperature and vertical-velocity fluctuations at $z = 100$ m in the whole outer domain: the nested region is marked by the square box. With two-way nesting, the inner-domain flow is averaged and put back to the outer domain at every time step of the outer-domain integration. Thus, the flow field shown inside the nested region is actually from the inner-domain LES. The simulated turbulent motion flows smoothly across the nest boundaries. For a more detailed comparison, we replot the same coarse-grid flow fields but only within the nested domain in the top panels of Fig. 6 and compare them to those generated from the nested LES (bottom panels of Fig. 6). As expected, the flow field in the overlapped region of the outer-domain LES is just a smoothed version of those in the nest domain. No noisy feature shows up along the nest boundaries. Both domains show the irregular cellular structure with the size of about the PBL depth, similar to those observed by Schmidt and Schumann (1989). As there should be, more hexagons are captured in the outer LES (Fig. 5), while more detailed structures are revealed in the nest LES (bottom of Fig. 6).

The turbulent statistics calculated from both domains show a similar behavior. The time evolution (between 8 and 15 t_*, where $t_* \equiv z_i/w_* \sim 650$ s is the large eddy turnover time) of the predicted surface heat flux (Q_0), convective velocity (w_*), and layer-averaged TKE is compared in Fig. 7. The surface heat flux is slightly larger in the outer domain but only by a few percent; this difference starts right after the nest domain is turned on, so it is likely due to the spinup process of the nest domain. The convective velocity is 1.5–1.7 m s^{-1} and the layer-averaged TKE (normalized by w_*^2) about 0.35 in both domains. The normalized turbulence intensity agrees well with that reported in Nieuwstadt et al. (1993). Because of the imposed strong capping inversion, the PBL did not grow significantly; the PBL height remains at ~1 km. (For simplicity, we use the initial PBL height z_{i0} to normalize the height coordinate for the profile statistics shown below.)

The vertical profiles of total and SGS heat fluxes, first normalized by its own Q_0 value and then averaged over the time period of 8–15 t_*, are given in Fig. 8a. As expected, the outer domain (solid curves) produces a larger SGS flux than the inner domain (dotted curves) but the total flux remains about the same between the two LESs. (The kinks in the total heat flux near the surface result from the fact that the WRF model uses a mass coordinate. To compute the flux requires performing data interpolation onto the height coordinate, which is hard to do near the surface where some first mass points are above the first height coordinate.) The

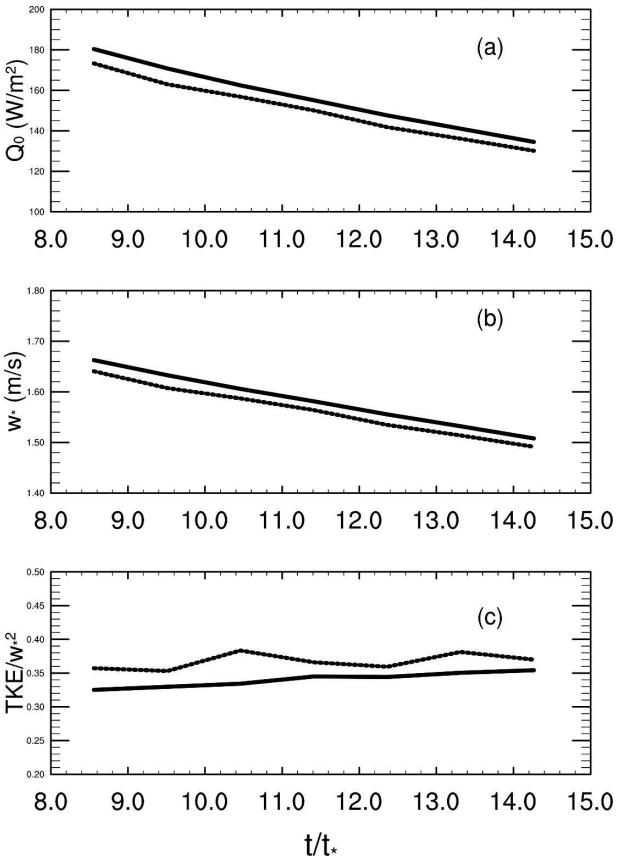

FIG. 7. Comparison of the time evolution of (a) surface heat flux, (b) convective velocity, and (c) layer-averaged TKE between the two LES domains form case F. The solid lines are calculated from the outer domain and dotted lines are from the inner domain.

flux profiles of the two domains are comparable to those without nesting shown in Fig. 1a. Again, both LESs produce an entrainment flux larger than $-0.2Q_0$.

The total velocity variances (RS plus SGS) are also similar between the outer and inner domains (Fig. 8b). Compared to the difference between the two single-domain runs shown in Fig. 1b, the variances produced from the two LESs with two-way nesting are more similar to each other; two-way nesting tends to bring the nested finer-grid solution closer to the outer-domain coarser-grid solution.

We may conclude here that the nested LES with lateral boundaries specified by the outer-domain LES flow behaves similarly to the LES with periodic boundary conditions in x and y from this free-convective PBL simulation.

b. *Friction velocity bias*

The neutral PBL run exposed a second problem that motivated our design of the two-part SGS eddy viscos-

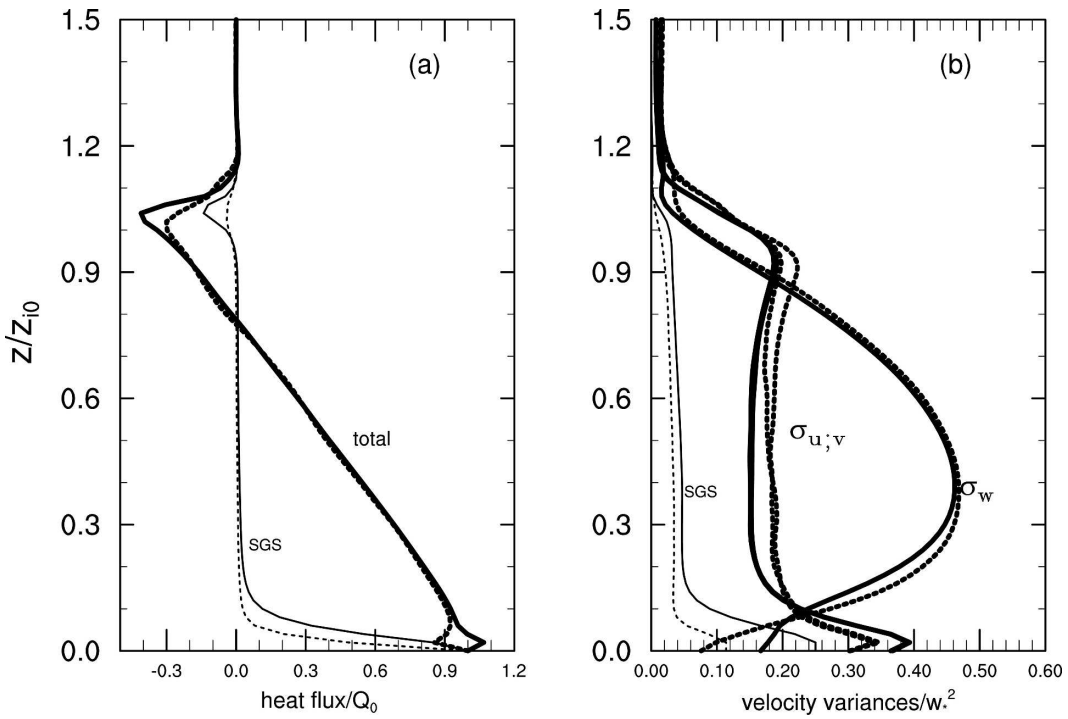

FIG. 8. Comparison of the vertical profiles of the time-averaged (a) heat flux and (b) velocity variances between the two LES domains from case F. The solid lines are calculated from the outer domain, dotted lines from the inner domain, thick lines are the total contributions (RS plus SGS), and thin lines are the SGS contributions.

ity model described in section 2c. We first simulated the shear case using the standard Smagorinsky SGS model and found that the friction velocity u_* was persistently smaller inside the nest domain compared to the outer domain; the horizontally averaged u_* is $\sim$0.4 m s^{-1} in the inner domain versus $\sim$0.5 m s^{-1} in the outer domain. The bias is evidenced in Fig. 9a, which shows the contours of the local friction velocity over the entire outer domain at the end of the simulation. The near-surface wind (Fig. 9b) is also consistently smaller in the nest region. (The mean wind speed at this level is about 4–5 m s^{-1}.) This wind bias is observed only very close to the surface (i.e., at the first 1–2 grid levels). This bias appeared only after we turned off the weak surface heating and it persisted throughout the whole simulation of the neutral PBL.

We identified the problem as follows. With different grid resolutions, the SGS momentum flux (based on Smagorinsky's model) near the surface is much smaller in the inner domain than in the outer domain as shown in Fig. 10a. Because near the surface the RS contributions are negligible, the total momentum flux (downward) is much smaller in the nest domain. This brings less momentum downward and yields a smaller near-surface wind. A weaker near-surface wind results in a smaller surface stress according to MO theory.

In a conventional LES without nesting, a smaller SGS in a finer-resolved LES is compensated for by more RS motions—even near the surface—so that the total flux remains insensitive to grid resolution, as demonstrated from previous LESs (e.g., comparing different resolution LESs reported in Andren et al. 1994; Moeng and Sullivan 1994; Sullivan et al. 1994). This insensitivity of u_* to grid resolution for conventional LESs is supported from the two single-domain WRF LES runs shown in Fig. 2; both LESs produce $u_* \sim 0.5$ m s^{-1} during the last hour of simulations. This indicates that the bias problem is related to grid nesting.

With nesting, if the surface wind and surface friction become smaller inside the nest domain, the pressure (or mass) field also responds to these differences and develops weaker fluctuations, as seen in Fig. 9c. This bias appears and persists also in one-way nesting of two different grid resolutions. It is not clear why the RS field inside the nest LES does not respond to the grid difference and compensate for the difference in the SGS stress near the surface, just like the single-domain LESs do. It may relate to the fact that the near-surface RS field in the nest LES is bounded by the nest boundary flow specified by the outer-domain LES.

To address this problem, we developed the two-part SGS model described in section 2c. As mentioned be-

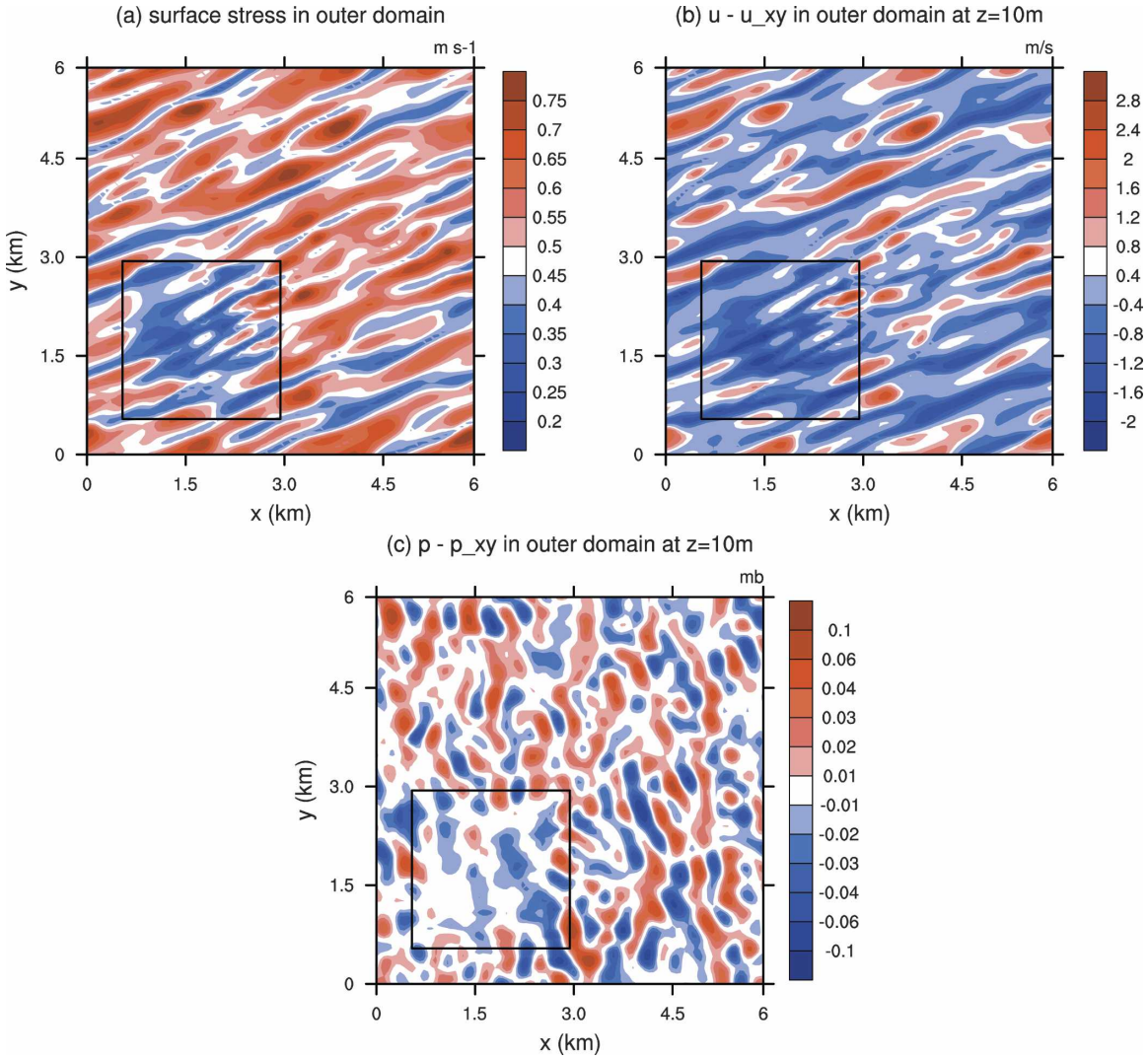

FIG. 9. Contours of (a) surface friction velocity, (b) u fluctuations at $z = 10$ m, and (c) p fluctuations at $z = 10$ m from the outer-domain simulation of case S using just the Smagorinsky SGS model.

fore, the Samgorinsky-type of SGS model is questionable near the wall region where few turbulent eddies are resolved. Near the wall, the SGS model is responsible for most of the ensemble-mean statistics, and hence should be grid-size independent there. The K_M^{wall} part of the eddy viscosity that we propose to augment the Smagorinsky model near the surface is grid-size independent, and thus effectively closes the gap between the near-surface SGS momentum fluxes of the two domains as seen in Fig. 10b. This leads to a similar amount of total momentum flux near the surface, and hence similar surface wind and friction velocity, in both domains.

Figures 11a,b plot the same variables as Figs. 9a,b, but are from the run with the new SGS model; the bias in the surface stress and near-surface wind fields disappears. In addition, we show the u fluctuations at $0.1z_i$ in Fig. 11c and higher up in Fig. 11d. The flow field reveals the streaky features that roughly align with the near-surface wind at $0.1z_i$ but the streaks disappear and are replaced with spatially less coherent structures at $0.5z_i$, just like those shown in Moeng and Sullivan (1994). Again, the simulated turbulent motion flows smoothly across the nest boundaries.

Figure 12 compares the time evolution of the layer-averaged (over $0 < z < 500$ m) TKE and the averaged surface friction velocity u_* between the two LES domains. Both LESs predict a total TKE level at about 3.5 u_*^2 during the last few hours of simulation. The horizontally averaged surface friction velocity is about 0.5 m s^{-1} toward the end of the simulation for both domains; this value compares reasonably with that from

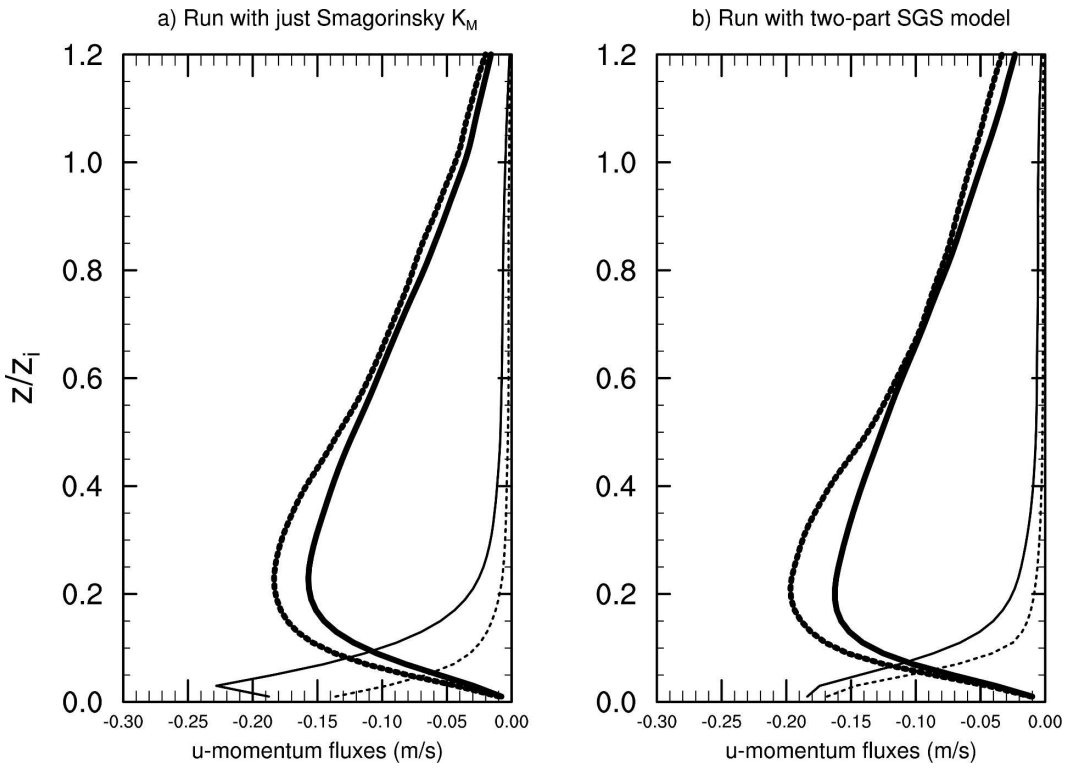

FIG. 10. Comparison of the u-momentum flux profiles between the two domains from case S where (a) the Smagorinsky SGS model is used and (b) the two-part SGS model is used. Solid lines are from the outer domain, dotted lines are from the inner domain, thick lines are the RS contributions, and thin lines are the SGS contributions.

previous LESs. (Moeng and Sullivan 1994 reported a time averaged u_* of 0.5 m s^{-1} while Sullivan et al. 1994 reported a time averaged value of 0.499 m s^{-1} with their baseline SGS and 0.536 m s^{-1} with their new SGS model.)

The three velocity variances (RS plus 2/3 of the SGS TKE) are given in Fig. 13. The difference in the u variance between the two LESs with two-way nesting are much smaller than that between the two single-domain different-resolution runs shown in Fig. 2b, showing that two-way nesting brings the nested finer-grid solution closer to the outer-domain coarser-grid solution.

4. Summary and discussion

To extend LES applications to real-world complex PBLs, we can no longer use periodic boundary conditions in x or/and y, as most PBL LESs do. One way to tackle the complex PBL problems in weather forecast models and also to allow for the feedback of the resolved turbulent motion on mesoscale events is to explicitly simulate both turbulent and mesoscale motions of interest through two-way nesting. But before adopting this approach, it is necessary to examine the capability of two-way horizontal nesting for turbulence simulation. To do so, we design a pair of LES-within-LES experiments where a finer-grid LES domain is nested inside a coarser-grid LES domain and both LESs are driven under the same environmental conditions. With the same uniform forcing, we expect the two LES flows to behave similarly in the statistical sense. Having the two domains interacting with each other is a strict test for the LESs' sensitivity to grid nesting and also to SGS modeling as differences in their statistical behavior will be amplified at the nest boundaries.

We perform these experiments using the WRF model framework. The outer-domain LES uses a periodic boundary condition in x and y just like a conventional PBL LES, while the inner-domain LES uses specified lateral boundary conditions based on the outer-domain flow. The intercomparison between the two LES solutions forms a base for validation. The use of two well-tested and well-documented PBL regimes (the horizontally homogeneous free-convective and neutral PBLs) provides another method of validation.

From these LES-within-LES experiments, we have learned the following.

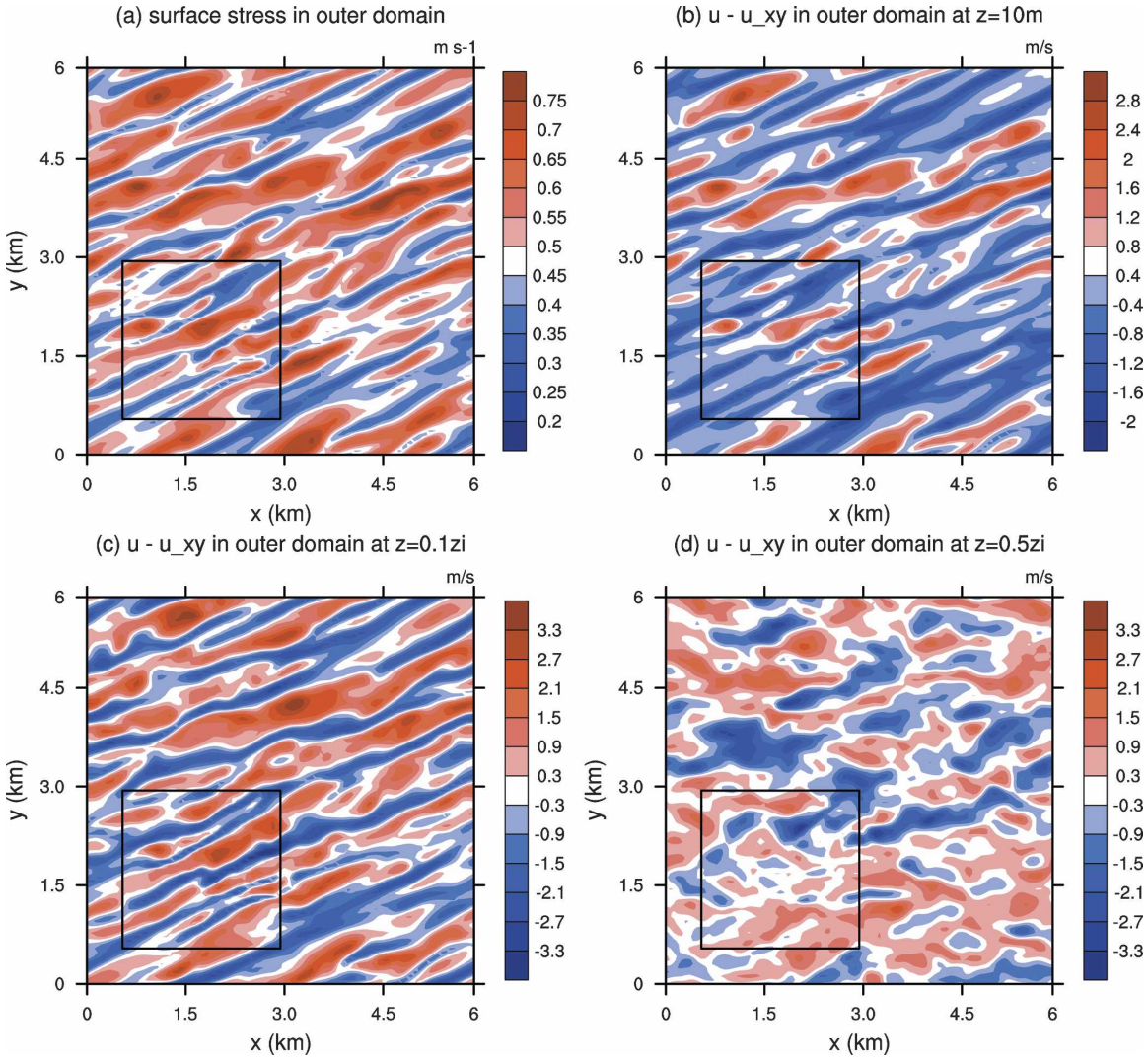

FIG. 11. Contours of (a) surface friction velocity, (b) u fluctuations at $z = 10$ m, (c) u fluctuations at $z = 0.1z_i$, and (d) u fluctuations at $z = 0.5z_i$ from the outer-domain simulation of case S using the two-part SGS model.

1) A relaxation zone (five grid cells in our experiments) along the nest boundaries is necessary to produce turbulent flows that smoothly blend across the two domains.
2) To prevent the need of specifying the SGS TKE at the nest boundaries, one can ignore the small advection term and solve the SGS TKE budget diagnostically.
3) The horizontal extent of the inner LES domain has to be large enough (larger than $5z_i$) to inhibit a mean temperature (and hence mean vertical velocity) bias between the two domains for the convective PBL.
4) To avoid the generation of a bias in surface friction (and near-surface wind) between the two domains, the traditional Smagorinsky SGS model needs to be modified. In this paper we develop a new two-part SGS model with an additional near-wall K_M that is grid independent. This modification prevents the surface-friction bias from occurring.

With the above modifications, the two-way nest LESs in the WRF framework can produce similar turbulent structure and statistics in both domains when driven by the same forcing. The simulated turbulent motion flows smoothly across the two domains with no apparent noisy features along the nest boundaries. The statistics (i.e., mean fields, fluxes, and variances) calculated from both LES domains also compare well with those derived from field measurements (e.g., Lenschow et al. 1980), laboratory data (e.g., Willis and Deardorff 1979), and previous LESs (e.g., Schmidt and Schumann

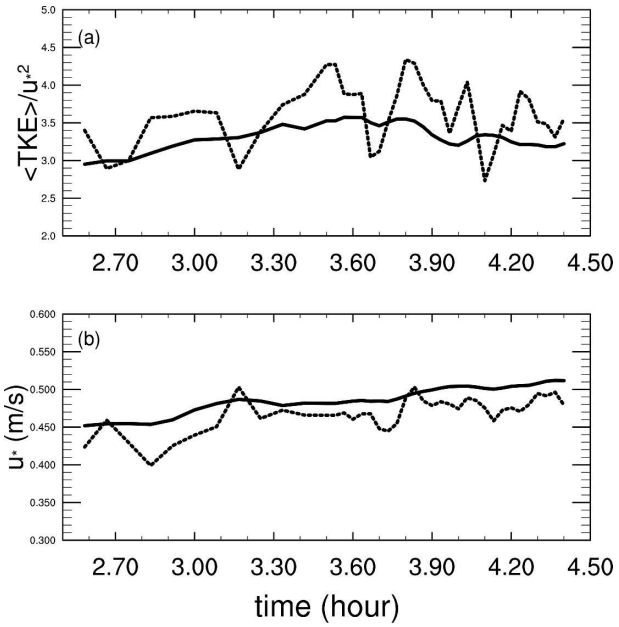

FIG. 12. Comparison of the time evolution of (a) layer-averaged TKE and (b) surface friction velocity between the two domains for case S using the two-part SGS model. Solid lines are from the outer domain and the dotted lines are from the inner domain.

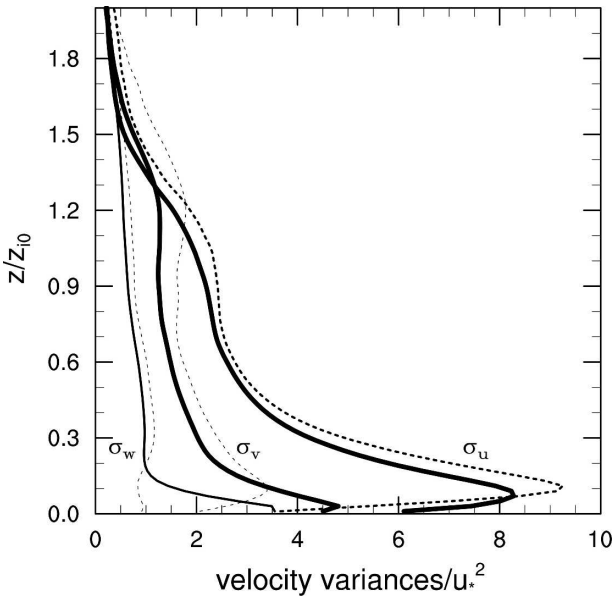

FIG. 13. Comparison of the velocity variances between the two LES domains from case S using the two-part SGS model. Solid lines are calculated from the outer domain and dotted lines are from the inner domain.

1989; Nieuwstadt et al. 1993; Moeng and Sullivan 1994; Andren et al. 1994; Sullivan et al. 1994). However, this WRF LES code still has the long-standing problem of law-of-the-wall deficiency in the surface layer for shear-driven PBL, and may overpredict the entrainment heat flux for the convective PBL; however, they are not nest-related problems.

Our experiments show that two-way nesting is feasible for LES-within-LES type of nesting. But nesting an LES inside a mesoscale model poses a much bigger challenge. As shown in this study, the SGS model must play a compensating role in order for both domains to produce the same amount of transport of heat and momentum under the same uniform forcing. In a mesoscale model the net turbulent transport is predicted from an ad hoc ensemble-mean 1D PBL parameterization. It is difficult, if not impossible, for any 1D PBL parameterization scheme to predict the turbulent transport as accurately as a 3D LES simulation. Thus, the mean temperature or wind field is likely to differ between the PBL in the mesoscale domain and the PBL in the nested LES domain even if both PBLs are driven by the same forcing. A careful design of subgrid mixing that blends the ensemble-mean PBL scheme to the LES type of SGS model is needed (Wyngaard 2004). Another challenge lies in the inflow lateral boundary conditions. Any specified flow along the nest boundaries based on a mesoscale model is laminar by construction, thus, creating turbulent spinup problems once it flows into the LES domain. How to best deal with this spinup process is unclear. Gradually scaling down from mesoscale to turbulence domains using multiple nests may be needed to tackle the above problems. Further complications due to complex terrain and clouds pose additional challenges for LES applications to real-world PBLs. All of these challenges should be explored systematically and carefully with idealized simulations, similar to the ones we have performed in this study. This LES-within-LES study based on two idealized PBLs serves only as a first step in this process.

Acknowledgments. We thank Wei Wang, Dave Gill, George Bryan, Bill Skamarock (all at NCAR), and Chris Golaz (GFDL) for their help.

REFERENCES

Andren, A., A. R. Brown, J. Graf, P. J. Mason, C.-H. Moeng, F. T. M. Niewstadt, and U. Schumann, 1994: Large-eddy simulation of a neutrally stratified boundary layer: A comparison of four computer codes. *Quart. J. Roy. Meteor. Soc.,* **120,** 1457–1484.

Chow, F. K., A. P. Weigel, R. L. Street, M. W. Rotach, and M. Xue, 2006: High-resolution large-eddy simulations of flow in a steep Alpine Valley. Part I: Methodology, verification, and sensitivity experiments. *J. Appl. Meteor. Climatol.,* **45,** 63–86.

Deardorff, J. W., 1972: Numerical investigation of neutral and unstable planetary boundary layers. *J. Atmos. Sci.,* **29,** 91–115.

——, 1974: Three dimensional numerical study of turbulence in an entraining mixed layer. *Bound.-Layer Meteor.,* **7,** 199–226.

——, 1980: Stratocumulus-capped mixed layer derived from a three-dimensional model. *Bound.-Layer Meteor.,* **18,** 495–527.

Doran, J. C., J. D. Fast, and J. Horel, 2002: The VTMX 2000 campaign. *Bull. Amer. Meteor. Soc.,* **83,** 537–551.

Fedorovich, E., E. T. M. Nieuwstadt, and R. Kaiser, 2001: Numerical and laboratory study of a horizontally evolving convective boundary layer. Part I: Transition regimes and development of the mixed layer. *J. Atmos. Sci.,* **58,** 70–86.

Germano, M., U. Piomelli, P. Moin, and W. H. Cabot, 1991: A dynamic subgrid-scale eddy viscosity model. *Phys. Fluids A,* **3,** 1760–1765.

Hadfield, M. G., W. R. Cotton, and R. A. Pielke, 1991: Large-eddy simulations of thermally forced circulations in the convective boundary layer. Part I: A small-scale circulation with zero wind. *Bound.-Layer Meteor.,* **57,** 79–114.

Juneja, A., and J. G. Brasseur, 1999: Characteristics of subgrid-resolved-scale dynamics in anisotropic turbulence, with application to rough-wall boundary layers. *Phys. Fluids,* **11,** 3054–3068.

Kravchenko, A. G., and P. Moin, 1997: On the effect of numerical errors in large eddy simulations of turbulent flows. *J. Comput. Phys.,* **131,** 310–322.

Lenschow, D. H., J. C. Wyngaard, and W. T. Penell, 1980: Mean-field and second-moment budgets in a baroclinic, convective boundary layer. *J. Atmos. Sci.,* **37,** 1313–1326.

Lin, C.-H., C.-H. Moeng, P. P. Sullivan, and J. C. McWilliams, 1997: The effect of surface roughness on flow structures in a neutrally stratified planetary boundary layer flow. *Phys. Fluids,* **9,** 3235–3249.

Mason, P. J., and D. J. Thomson, 1992: Stochastic backscattering in a large-eddy simulations of boundary layers. *J. Fluid Mech.,* **242,** 51–78.

Mayor, S. D., P. R. Spalart, and G. J. Tripoli, 2002: Application of a perturbation recycling method in the large-eddy simulation of a mesoscale convective internal boundary layer. *J. Atmos. Sci.,* **59,** 2385–2395.

Moeng, C.-H., 1984: A large-eddy-simulation model for the study of planetary boundary-layer turbulence. *J. Atmos. Sci.,* **41,** 2052–2062.

——, and J. C. Wyngaard, 1988: Spectral analysis of large-eddy simulations of the convective boundary layer. *J. Atmos. Sci.,* **45,** 3575–3587.

——, and P. P. Sullivan, 1994: A comparison of shear-and buoyancy-driven planetary boundary layer flows. *J. Atmos. Sci.,* **51,** 999–1022.

——, and ——, 2003: Large eddy simulation. *Encyclopedia of Atmospheric Sciences,* J. R. Holton, J. A. Curry, and J. A. Pyle, Eds., Academic Press, 1140–1150.

Nieuwstadt, F. T. M., P. J. Mason, C.-H. Moeng, and U. Schumann, 1993: Large-eddy simulation of the convective boundary layer: A comparison of four computer codes. *Turbulent Shear Flows 8,* F. Durst et al., Eds., Springer-Verlag, 431 pp.

Patton, E. G., P. P. Sullivan, and C.-H. Moeng, 2005: The influence of idealized heterogeneity on wet and dry planetary boundary layers coupled to the land surface. *J. Atmos. Sci.,* **62,** 2078–2097.

Porte-Agel, F., C. Meneveau, and M. B. Parlange, 2000: A scale-dependent dynamic model for large-eddy simulation: Application to a neutral atmospheric boundary layer. *J. Fluid Mech.,* **415,** 261–284.

Rotach, M. W., and Coauthors, 2004: Turbulence structure and exchange processes in an Alpine Valley: The Riviera Project. *Bull. Amer. Meteor. Soc.,* **85,** 1367–1385.

Schmidt, H., and U. Schumann, 1989: Coherent structure of the convective boundary layer derived from large-eddy simulations. *J. Fluid Mech.,* **200,** 511–562.

Skamarock, W. C., J. B. Klemp, J. Dudhia, D. O. Gill, D. M. Barker, W. Wang, and J. G. Powers, 2005: A description of the advanced research WRF version 2. NCAR Tech. Note NCAR/TN-468+STR, 88 pp.

Sullivan, P. P., J. C. McWilliams, and C.-H. Moeng, 1994: A subgrid-scale model for large-eddy simulation of planetary boundary-layer flows. *Bound.-Layer Meteor.,* **71,** 247–276.

——, ——, and ——, 1996: A grid nesting method for large-eddy simulation of planetary boundary-layer flows. *Bound.-Layer Meteor.,* **80,** 167–202.

Takemi, T., and R. Rotunno, 2003: The effects of subgrid model mixing and numerical filtering in simulations of mesoscale cloud systems. *Mon. Wea. Rev.,* **131,** 2085–2101.

Willis, G. E., and J. W. Deardorff, 1979: Laboratory observations of turbulent penetrative-convection platforms. *J. Geophys. Res.,* **84,** 295–302.

Wyngaard, J. C., 2004: Toward numerical modeling in the "terra incognita." *J. Atmos. Sci.,* **61,** 1816–1826.